

Article

Mapping of a Novel Zero-Liquid Discharge Desalination System Based on Humidification–Dehumidification onto the Field of Existing Desalination Technologies

Sebastian A. Romo ^{1,*} , Mohammed Elhashimi ² , Bahman Abbasi ²  and Jelena Srebric ¹ ¹ Department of Mechanical Engineering, University of Maryland, College Park, MD 20742, USA² School of Mechanical, Industrial, and Manufacturing Engineering, Oregon State University, Corvallis, OR 97331, USA

* Correspondence: sromo1@umd.edu

Abstract: It is well-established that increasing demands for fresh water are paving the way for desalination technologies. However, this correlates with an increase in brine production whose treatment and disposal can be complicated and expensive. This paper presents a thermodynamic model to bound the operation and development of a novel Humidification–Dehumidification-based system featuring Zero-Liquid Discharge and off-grid capabilities. The model employs conservation laws to find feasible state points to meet a baseline operation of 10 kg/h of product water separated from a hypersaline feed stream with 100 g/kg salt concentration. The system incurs in a 1039 kWh/m³ energy intensity that can be supplied completely by an electric source or in combination with heating steam. Follow-up sensitivity analysis highlights the robustness of the system in handling variations of 25% in product flowrate and 75% in feed salinity, practically without incurring any additional energy demands. The proposed system operating costs between 72 USD/m³ and 96 USD/m³ are comparable to those of existing brine disposal techniques. Furthermore, an operational map of existing desalination technologies suggests a niche characterized by high recovery rates and high feed salinities that are generally unfulfilled by conventional desalination methods. Overall, the proposed system shows potential for off-grid hypersaline brine treatment. This study sets the stage for future development of physics-based and data-driven predictive models as the proposed system iterates into a pilot plant deployment.

Keywords: zero-liquid discharge; humidification–dehumidification; hypersaline brine; off-grid; brine management; thermal desalination; hybrid desalination plants



Citation: Romo, S.A.; Elhashimi, M.; Abbasi, B.; Srebric, J. Mapping of a Novel Zero-Liquid Discharge Desalination System Based on Humidification–Dehumidification onto the Field of Existing Desalination Technologies. *Water* **2022**, *14*, 2688. <https://doi.org/10.3390/w14172688>

Academic Editor: Andrea G. Capodaglio

Received: 27 July 2022

Accepted: 25 August 2022

Published: 30 August 2022

Publisher's Note: MDPI stays neutral with regard to jurisdictional claims in published maps and institutional affiliations.



Copyright: © 2022 by the authors. Licensee MDPI, Basel, Switzerland. This article is an open access article distributed under the terms and conditions of the Creative Commons Attribution (CC BY) license (<https://creativecommons.org/licenses/by/4.0/>).

1. Introduction

Desalination systems, as a vital infrastructure, need innovations focused on their production capabilities, adaptation to site-specific factors such as feed-water characteristics or available energy type, and operation issues that compromise performance [1,2]. Within the latter, fouling and brine discharge are two serious and recurrent problems in the operation of both membrane-based and thermal desalination systems that reduce performance and incur significant costs [3–5]. Reverse Osmosis (RO) is the most important membrane-based technology, which consumes a relatively small amount of energy per product flow rate [6,7], but it is consistently challenged by fouling problems [8,9]. Fouling can be organic, inorganic (scaling), biological, oxidization, or other types [10]. Fouling leads to increases in the required pumping power [11,12] and can account for 11–24% of the total operating expenses [13]. This generally limits the membrane-based technologies to an average threshold of feed salinity and recovery to stay competitive [14]. Although still present, fouling is less impactful in thermal desalination processes [15,16]. Thermal methods, such as Multi-Effect Distillation (MED) and Multi-Stage Flash, consume larger amounts of energy per product flow rate compared to the RO consumption. Therefore,

the thermal desalination methods are associated with higher production costs than the membrane-based molecular transport methods [6]. Scaling limits feed-water quality to brackish and seawater salinities, making it unsuitable to treat local high-salinity water [14]. Therefore, the treatment of high-concentration brines remains an unviable investment in many cases.

In desalination, the water product is usually separated from the feed stream, and the remaining water is discharged as brine. Brine disposal can be problematic due to high salinity and, in the case of thermal desalination, elevated temperatures. This can have severe impacts on both ground and marine environments due to pollution and sometimes toxicity [17]. Therefore, strict environmental regulations govern and limit brine discharges in many different locations around the world [18]. Zero-Liquid Discharge (ZLD) is an attractive alternative to brine disposal, as the only process byproduct is solid salt. However, the only practical and scalable implementations of ZLD consist of brine post-treatment through mechanical crystallizers and evaporation ponds [14]. In the first option, a brine crystallizer is an additional device that further desalinates the brine stream by gradually flashing vapor until salt crystals form. Besides an additional capital expense for brine crystallizer systems, pumping the viscous sludge can incur high operation costs that make this option economically unviable [14,19]. Evaporation ponds, while having small operation expenses, require large land areas and time for brine processing [20].

A novel humidification–dehumidification (HDH) water desalination technology with ZLD has a potential to solve problems associated with fouling, brine discharge, and decentralization, so it was conceptually embodied in a Solar Thermal Extraction of Water by Atomization and Recuperative Desalination (STEWARD) system [21]. The use of humidification–dehumidification should make the STEWARD system less sensitive to fouling and should also allow the potential use of low-grade energy, such as solar energy and industrial waste heat [22,23]. The HDH-ZLD process within the STEWARD system currently has ongoing research efforts focused on component-based investigations of the rates of humidification [24], atomizer design [25], and centrifugal salt separation [26]. Therefore, the present study focused on first-principles analyses of these system components and further modeled the performance of a complete system to enable mapping of potential operational ranges onto the operational field of existing desalination technologies. Specifically, the contributions of this study are:

- A mathematical model for the proposed STEWARD system used to bound operational space through physical conservation laws and to estimate the thermodynamic states at each point of the desalination process;
- A sensitivity analysis highlighting the engineering tradeoffs associated with variations in product flow rate and feed salinity;
- An evaluation of the practical implications related to deploying the STEWARD system to potentially replace existing desalination plants or complement brine processing;
- Identification of deployment opportunities for STEWARD within the current operational space of existing desalination technologies.

The paper first presents descriptions of the STEWARD system, associated modeling equations, and simulation algorithm. Afterwards, the paper presents the simulation results of a baseline operation and sensitivity analysis. Furthermore, the paper discusses practical implications of deploying the STEWARD system to potentially replace existing systems or supplement brine processing in actual desalination facilities. Finally, this HDH-ZLD system is mapped onto the operational space of existing desalination technologies to identify the technical niche in which it could potentially be deployed.

2. Methodology

This section explains the underlying thermodynamic process of the STEWARD system and disseminates the key equations that describe its operation. The simulation challenges related to calculating the thermodynamic state after atomization are explained, as well as the modeling constraints and algorithm employed by the proposed model.

2.1. Overall System Description

Figure 1 shows a schematic of the novel desalination system modeled in this work. At point (1), near-stagnant air enters a compressor where it is compressed. The stream leaves through hot-air jets (2) used to atomize a thin saline water film. Atomizing saline water with salinity higher than 100,000 ppm (typical RO discharge salinity) using conventional atomizers is a challenge, as scaling can clog any orifices in very short time periods [24]. A novel atomizer design (3) is implemented to suppress the fouling and sustain the cycle [25]. The next stage is the heat exchange, which consists of a double-phase heat exchanger (evaporator/condenser) and a first heat recuperation stage. The fine spray generated by the atomizer is fully evaporated and absorbed by the carrier dry air. To stay economically viable, the maximum energy needs to be recuperated in this heat exchanger. For that, the boundary conditions need to be accurately pinpointed. Before entering the evaporator, the dry air is slightly humidified by the partial evaporation of the saline water. Conventional analytical models fail to pinpoint the thermodynamic state at this point, as it is a multi-constraint optimization problem. The constraints of mass and energy continuities and maximization of entropy are not sufficient to solve the problem. Additional constraints from the working cycle need to be introduced.

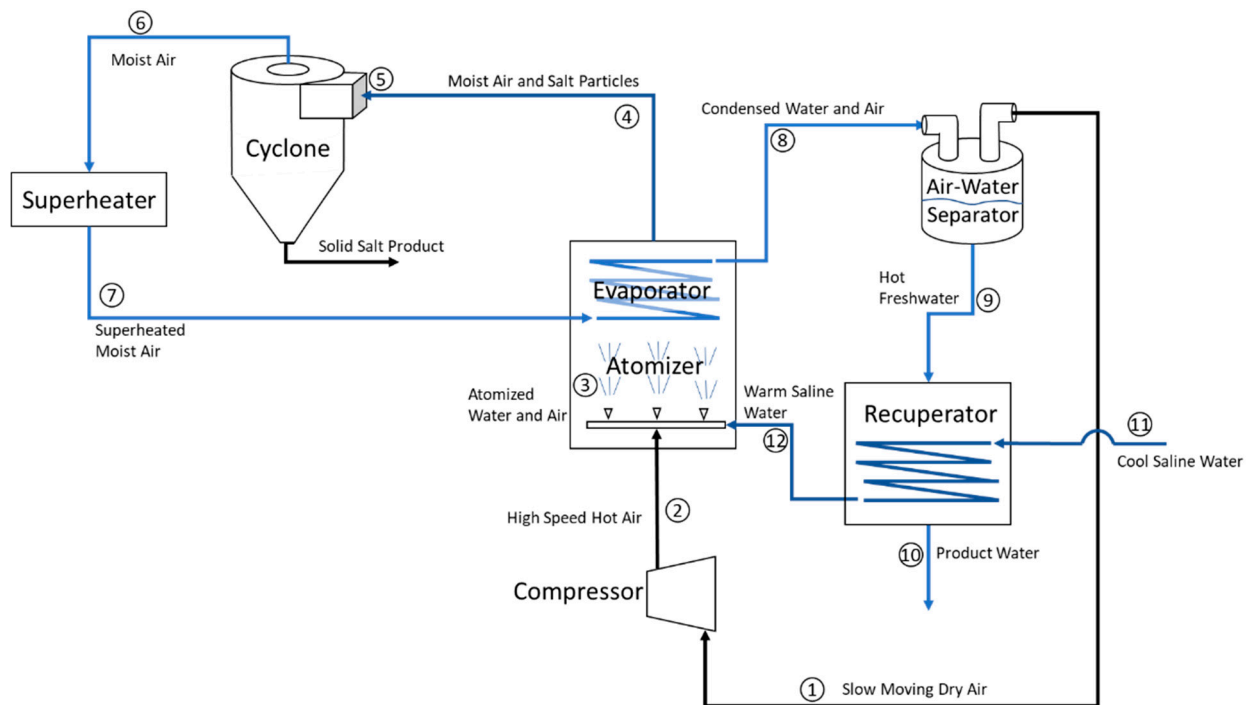


Figure 1. Diagram schematic of the proposed system.

After the heat exchanger (4), a homogenous mixture of moist air and salt crystals enters a cyclone separator (5), which is another potential choking point in the cycle. Analytical, numerical, and experimental investigations proved how the cyclone separator has a high resistance to fouling [26]. The continuous salt separation in the solid phase coupled with the nature of the HDH makes the technology resistant to fouling. The clean humid air (6) then enters a superheater, which uses low-grade thermal energy to introduce additional energy to the system and prevents premature condensation prior to the condenser. The hot moist air then enters the condenser side, where it recoups the sensible and latent heats to evaporate the sprays in the evaporator side. Then, a mixture of almost dry air (down to the thermodynamic limit) and liquid water exits the condenser (8). This mixture enters an air–water separator, after which the air recirculates in the cycle. At some operating conditions, the warm fresh water could potentially be used to preheat the incoming streams of saline water.

2.2. Model Description

A significant challenge in the proposed design lies in bounding the thermodynamic state of the atomized water-and-air mixture for plausible operation. To achieve this, an iterative algorithm is employed that tests all the possible temperature-relative humidity combinations and eliminates physically nonviable options through checkpoints along the evaporator, cyclone, superheater, and condenser loop. The pressure loss of atomization is determined to be around 50 kPa at the operating flow rates [24]; the possible temperature range is bounded by the water and air temperatures, T_{12} and T_2 , respectively; and finally, the possible relative humidity range is between 0 and 100%. Each iteration consists in setting a temperature value from the range and trying all possible relative humidity range values and eliminating the combinations that do not pass the following checkpoints:

- The partial pressure of water ($P_{3,w}$) is defined by T_3 and ϕ_3 , which must be lower than P_3 to result in a positive humidity ratio:

$$W_3 > 0; \quad (1)$$

- State 4 is calculated through an iterative algorithm that finds T_4 such that the resulting humidity ratio W_4 matches that of full evaporation of the warm saline water stream (m_{12}/m_2). To guarantee heat transfer and full evaporation, T_4 must be slightly greater than T_3 , and thus, the checkpoint follows that:

$$T_4 - 0.5 > T_3; \quad (2)$$

- It has been determined that expansion cooling of the gas and cooling of the liquid through heat transfer are minimal during atomization processes, especially at fast discharges [27]. Therefore, the total enthalpy of the high-speed hot air and warm saline water streams before and after atomization mixing must remain equal or slightly lower due to losses in local evaporation and breaking of water droplets. The implemented checkpoint therefore ensures that H_3 is between 0 and 8% lower than the addition of the enthalpies in the streams preceding the atomizer such that:

$$\frac{(H_2 + H_{12}) - H_3}{(H_2 + H_{12})} < 0.08; \quad (3)$$

- The superheated moist air temperature is an input to the model and must be larger than the calculated temperature at the evaporator outlet per the second law of thermodynamics. Furthermore, the temperature at the evaporator outlet must be lower than the temperature of the condensed water-and-air stream leaving the condenser. Therefore, the implemented checkpoint verifies that:

$$T_4 < T_7, \quad (4)$$

and

$$T_8 < T_7; \quad (5)$$

- The heat available on the condensing side of the evaporator Q_c must be greater than the heat required to complete evaporation Q_e . This condition checks that at minimum:

$$Q_c > Q_e. \quad (6)$$

All possible atomized water and air (state 3) points that pass all the checkpoints are stored in an array. The most plausible state point is finally selected using the uniformly weighted ranking criteria based on three parameters: difference between available and required heat across the evaporator, entropy increase through atomization, and total enthalpy difference before and after atomization. At this stage in the simulation, the identified thermodynamic state points following atomization, at the equal or greater heat available in

the condensing side of the evaporator, have to achieve full evaporation of the atomized water stream. The model bounds the design space by selecting the point associated with the minimum difference between heat available and heat required in the evaporator. Furthermore, the model considers the atomized water-and-air state point that results in the largest entropy after atomization to implement a worst-case scenario design for safety in thermodynamic performance. Finally, the design is bounded by considering the lowest difference in total enthalpy of the air and water streams before and the combined stream after atomization. This assumes an optimized atomizer design with high discharge, which uses the air velocity for atomizing the water stream without incurring major thermodynamic losses [27].

The complete set of model equations for the desalination system are shown in Table 1. After determining the thermodynamic state point of the atomized water-and-air stream, the model continues calculations through the air–water separator and the recuperator. The state points at the recuperator inlets and outlets are calculated using the warm saline water state point 12, the temperatures of the cool saline water intake and hot freshwater streams at points 11 and 9, respectively, and a heat exchanger effectiveness of 0.8 as design constraints.

Table 1. Model Key Equations.

Component	Equation	Equation Number	Variables
Compressor	$W_{isen} = m_1 \left(\frac{\gamma_1}{\gamma_1 - 1} \right) P_1 \left(\frac{1}{\rho_1} \right) \left[\left(\frac{P_2}{P_1} \right)^{\left(\frac{\gamma_1 - 1}{\gamma_1} \right)} - 1 \right]$	(7)	W_{isen} Compressor power, isentropic m_1 Slow-moving dry-air mass flow rate γ_1 Isentropic ratio P_1 Inlet pressure
	$W_{comp} = \frac{W_{isen}}{\eta_{c,isen}}$	(8)	P_2 Outlet pressure W_{comp} Actual compressor power $\eta_{c,isen}$ Compressor isentropic efficiency
Evaporator	$Q_e = m_{3,sw} \lambda_{3,sw} + (m_{3,w} + m_{3,a}) c_{p,ma} (T_4 - T_3)$	(9)	Q_e Heat required for full evaporation $m_{3,sw}$ Saltwater flow rate $\lambda_{3,sw}$ Saltwater latent heat of vaporization $m_{3,w}$ Water-vapor flow rate $m_{3,a}$ Air flow rate $c_{p,ma}$ Specific heat capacity of moist air T_4 Outlet temperature T_3 Inlet temperature
Superheater	$dH_{sup} = m_w (h_{7,w} - h_{6,w}) + m_a (h_{7,a} - h_{6,a}) + m_s (c_{p7s} T_7 - c_{p6s} T_6)$	(10)	dH_{sup} Superheat enthalpy difference m_w Water-vapor mass flow rate $h_{7,w}$ Water-vapor enthalpy at superheat temp. $h_{6,w}$ Water-vapor enthalpy at vapor saturation $m_{7,a}$ Dry-air mass flow rate $h_{7,a}$ Air enthalpy at superheat temp. $h_{6,a}$ Air enthalpy at saturation temp. $m_{7,s}$ Solid-salt mass flow rate c_{p7s} Specific heat capacity of solid salt T_7 Superheat temp. T_6 Saturation temp.
Condenser	$dH_{sat} = m_w (h_{6,w} - h_{8,w}) + m_a (h_{6,a} - h_{8,a})$	(11)	dH_{sat} Condensation enthalpy difference $h_{8,w}$ Water-vapor enthalpy at liquid saturation $h_{8,a}$ Air enthalpy at saturation temp.
	$Q_c = dH_{sup} + dH_{sat}$	(12)	Q_c Condensation heat
Cyclone	$P_6 = P_5 - dP_{cy}$	(13)	P_6 Outlet pressure P_5 Inlet pressure dP_{cy} Cyclone pressure drop
	$m_s = m_{5,s} \eta_{cy}$	(14)	m_s System-salt flow rate $m_{5,s}$ Inlet-salt flow rate η_{cy} Collection efficiency

The cyclone effects are modeled through the pressure drop (dP_{cy}) it incurs in the moist air flow and the collection efficiency (η_{cy}), which dictates the percentage of salt particles that are removed from the stream. The modeling approaches for pressure drop and collection efficiency are detailed to great extent in the literature [28,29]. A model that

considers cyclone dimensions, inlet thermodynamic state, flow velocity, and salt particle characteristics was initially implemented to size the component. Nevertheless, preliminary design experiments for the desalination system showed that these modeling approaches generally overestimated the pressure drop, likely due to the small size of the required cyclone, and that the achieved collection efficiency was consistently 0.99 or higher [26]. Experiments at the cyclone component level were conducted in a separate study [30]. For tests with dry-air flow rates of 10.8, 7.2, and 14.8 kg/h resulting in inlet velocities of 7.8, 5.7, and 10.7 m/s, with salt content (wt% of dry air) of 7.4, 9.7, and 10.8%, the experimentally measured collection efficiencies were 1, 0.998, and 0.997 with a maximum pressure drop of 200 Pa. In a test integrating the cyclone with the STEWARD system, separation efficiencies between 0.995 and 0.999 were observed for humid-air flow rates ranging from 3.6 to 16.2 kg/h, with inlet velocities between 10.1 and 32.7 m/s, humidity ratios ranging from 0.16 to 0.5, and intake salinities ranging from 35 to 150 g/kg. Thus, in our analysis, we conservatively assume a constant dP_{cy} of 5 kPa pressure drop and η_{cy} of 0.99.

The presented model has two major assumptions: a) constant cyclone separation efficiency and b) constant pressure drops across system components. The first major assumption consists of a constant cyclone efficiency of 0.99; this is a slightly conservative assumption justified by experimental results for intake salinities ranging from 25 g/kg to 147 g/kg where the separation efficiencies remained between 0.995 and 0.999 [30]. The second major assumption includes constant pressure drops across system components being: 50 kPa for atomization (process 2–3), 15% of the total pressure during evaporation (process 3–4), 5 kPa for the pressure drop across the cyclone (process 5–6), and 15% of the total pressure for condensation (process 7–8). These assumptions are justified by experimental data for each separate system component. Specifically, the atomizer air-side 50 kPa pressure drop is assumed as a design target for the ongoing atomizer development. Experimental results on a novel perforated-plate airblast atomizer for saline water at the corresponding air flow rate show about 150 kPa pressure drops [31]. However, the pressure drop can be significantly reduced through different atomizer design avenues. The pressure drop in effervescent atomization, for instance, at similar water flow rates can be as low as 25 kPa [32]. A combination of effervescent and airblast atomization can operate with air pressures ranging from 15 to 180 kPa [33]. Novel pneumatic atomizer designs can achieve atomization with less than 10 kPa pressure drop in the air stream, and 1.2 kPa in the water stream [34]. It must be noted that the water stream in the presented system serves two purposes: atomization, and a medium through which to transport water. Therefore, the energy required for atomization could further be reduced by assisting atomization with ultrasonic atomizers [35–37], while bypassing the necessary air flow to maintain moisture absorption and release. The cyclone pressure drop is experimentally determined to be negligible compared to the other component pressure drops [30]; therefore, the assumption of a 5 kPa is a conservative assumption that at this stage in design can be regarded as a worst-case scenario. The assumptions for pressure drop for both the evaporator and condenser sides correspond to the maximum pressure drops required to achieve the humidification rates for the baseline product-water flow rate. Although preliminary experiments on different heat exchanger design suggest lower pressure drops, we implement a conservative scenario for energy consumption calculations. Finally, the model assumes an air stream pressure of 48 kPa (state 1), and thus, any excess pressure is released in the air–water separator. This is a conservative assumption, as it has been determined that the pressure across the air–water separator pressure is within the ranges of 0.5 to 1.5 kPa [38], and thus leaves a safety margin for further optimization as the system is integrated into a pilot plant.

Moist air properties with temperature, pressure, and humidity dependence are calculated using the AirProperties MATLAB library [39], which is based on published correlations [40,41]. Dry air thermodynamic properties are calculated using the IdealAir MATLAB package [42]. Most saline and pure water properties are calculated using the Thermo-

physical Properties of Seawater library [43,44], and two-phase vapor-steam properties are calculated using the XSteam library [45]. Both XSteam and the Seawater libraries, however, could be used interchangeably at zero salinity.

3. Results

This section presents the simulation results at baseline operations and the underlying thermodynamic cycle of the system to find critical processes and components. A subsequent sensitivity analysis is presented by parametrizing product flow rate and feed salinities to understand the operational tradeoffs inherent to the system.

3.1. Baseline Operation

Table 2 shows the complete input set for simulation. The presented HDH- ZLD system employs a thermal process to drive desalination; however, it additionally features an air compressor driven by electric energy. In this analysis, we assume a scenario in which the superheater is driven by motive steam at the saturation pressure (P_s) corresponding to the superheated temperature, and another scenario where we assume an electric superheater. The compressor is always considered in the total energy consumption, as it incurs significant energy requirements within the process.

Table 2. Model Inputs—Baseline.

General Inputs	
Product flow rate, M_d (kg/s)	0.0027
Intake salinity, C_f (g/kg)	100
Intake temp., T_{in} (°C)	18
Family Inputs	
Motive steam pressure, P_s (kPa)	200
Specific Inputs	
Superheat temp., T_{sup} (°C)	120
Slow-moving dry-air pressure, P_1 (kPa)	48
Slow-moving dry-air temp., T_1 (°C)	20
Slow-moving dry-air rel. hum., ϕ_1 (–)	0.63
Air flow rate, m_1 (kg/s)	0.0054
High-speed hot-air pressure, P_2 (kPa)	150
Warm saline-water temperature, T_{12} (°C)	20

Table 3 shows the outputs of the simulation of the proposed system at baseline operation. The results show the most feasible operation point that follows the physical conservation laws. Thus, practically complete water recovery can be achieved from a considerably high feed-water salinity through the proposed system. Although the total specific energy consumption is large, it must be noted that roughly 10% of the required heat for evaporation is an external thermal input through the superheater. This translates to a high gain ratio that may not be an accurate metric of thermal performance as it is with other thermal desalination systems driven by a single energy input. This is a considerable difference from other thermal desalination systems, such as conventional HDH and MED, in which the heat required for desalination is completely supplied externally or partially supplemented by recirculated product steam in the case of energy recovery devices [46]. Instead, the proposed STEWARD system offsets the evaporation load to the compressor, which uses air to provide energy for increasing the surface area of evaporation of the water through atomization, absorbing moisture, and transferring heat through psychrometric processes.

Table 3. Model Outputs—Baseline.

General Outputs	
Product flow rate, M_d (kg/s)	0.0027
Feed-water flow rate, M_f (kg/s)	0.003
Brine flow rate, M_b (kg/s)	n/a
Product-water salinity, C_p (g/kg)	1
Feed-water salinity, C_f (g/kg)	100
Brine salinity, C_b (g/kg)	n/a
Actual recovery ratio, R	0.91
Family Outputs	
Specific energy, E_{des} (kWh/m ³)	Scenario 1: 986 _{el} , 53 _{th} Scenario 2: 1039 _{el}
Motive-steam flow rate, M_p (kg/s)	2.37×10^{-4} /n/a
Gain ratio, GR	11.4/n/a
Sp. cooling-water flow rate, sM_{cw} (kg/kg)	n/a
Specific Outputs	
Atomized water-and-air temp., T_3 (°C)	75
Atomized water-and-air rel. hum., ϕ_3 (–)	0.69
Solid salt-product flow rate., m_s (kg/s)	2.94×10^{-4}
Compressor power, W_{comp} (kW)	9.6
Evaporator heat required, Q_e (kW)	3.3
Condenser heat available, Q_c (kW)	7.3
Superheater heat, dH_{sup} (kW)	0.5

Some conventional performance indicators, such as gain ratio or specific cooling-water flow rate, do not completely apply in the proposed STEWARD system. Therefore, analyzing each of the cross-comparison hierarchies can provide a systematized method to assess its operation space and cycle characteristics through both energy supply scenarios. At the General Outputs level, the STEWARD system does not have a brine flow rate or salinity. Instead, almost 100% of the salt content is separated in the cyclone and rejected as a solid salt product. Considering the feed salinity of 100 g/kg, 0.0003 kg/s from the feed-water flow rate is part of the solid salt product. The actual recovery ratio is calculated with the ratio of product-water mass flow rate to total feed-water mass flow rate, which includes the mass of salt. Therefore, baseline recovery ratio is practically very close to 1, which is usually achievable only at low salinities with conventional desalination systems, such as Multi-Effect Distillation or RO [47]. The results show viability for hypersaline water with a feed concentration of 100 g/kg, which is generally out of range for conventional desalination applications.

The Family Outputs highlight a discrepancy in operation between conventional thermal desalination and the proposed method. The system does not have a cooling water to reject excess heat from the warm freshwater product. Heat losses in the air–water separator and the similar mass flows of hot and cold streams across the heat exchangers can make the need for a rejected cooling-water stream redundant. The motive-steam flow rate is considerably low in comparison to conventional Humidification–Dehumidification systems [48–50], which leads to a higher gain ratio as the external heat input is only required for the superheat portion of the evaporation curve. The specific energy required by the outlined process is fairly high but roughly within the order of magnitude of the energy intensity reported across the literature [47]. Although the separation phenomena in this system are driven by a thermal process, the superheat input can be electric, and thus, the system can be compared to the molecular transport desalination methods at an energy source level. The total electric input including superheater and compressor loads of baseline operation is 1039 kWh/m³. The total thermal load of ~50 kWh/m³ is similar to that reported in other hypersaline-brine desalination systems [51].

The parameters within the Specific Outputs category emphasize the importance of the evaporator design given the important constraints of the required flow and heat exchange. The superheat portion of the cooling–dehumidification process that takes place in the heat exchanger accounts for roughly 7% of the heat available. Superheat temperature, nevertheless, is required in the system, as it provides important control of the heat exchange pinch point and, thus, overall system performance. One of the checkpoints to evaluate the atomized water-and-air state before the evaporator (state point 3) checks that the heat available through the condensation of the superheated stream exceeds the heat required to achieve full evaporation. The results show that the heat available in the condenser side exceeds the required heat by the evaporator. While some improvements could occur to minimize this difference, a small excess available heat could make the system robust to changes in M_d and C_f .

Figure 2 shows the T-P diagram for baseline operation. The greatest temperature–pressure differential takes place during the compression of slow-moving dry air (state 1) at 20 °C. This process represents the greatest energy input to the system. The conditions for state point 2 are defined by the minimum flow velocity required for atomization considering the dynamic pressure losses in the atomizer and heat exchanger such that the target 21 m/s at the cyclone inlet is met to achieve >99% separation of salt particle sizes in the range of (100–350) μm . This target velocity is the median value of the velocity ranges measured during system tests [30]. An advantage of the presented system is that the water-absorbing capabilities of air are accentuated through the temperature increase in the air stream as a side effect of the compressor. Simultaneously heating the air and water stream within HDH systems has been found to increase overall performance [37]. This would favor the saline-water preheating through the recuperator and eliminate the need for cooling water that is discarded after preheating, as occurs in Thermovapor Compression (TVC), MED, and conventional HDH methods. In the water stream, the cool saline intake water (state 11) at 18 °C is preheated to become a warm saline water input at 20 °C (state 12) to the atomizer.

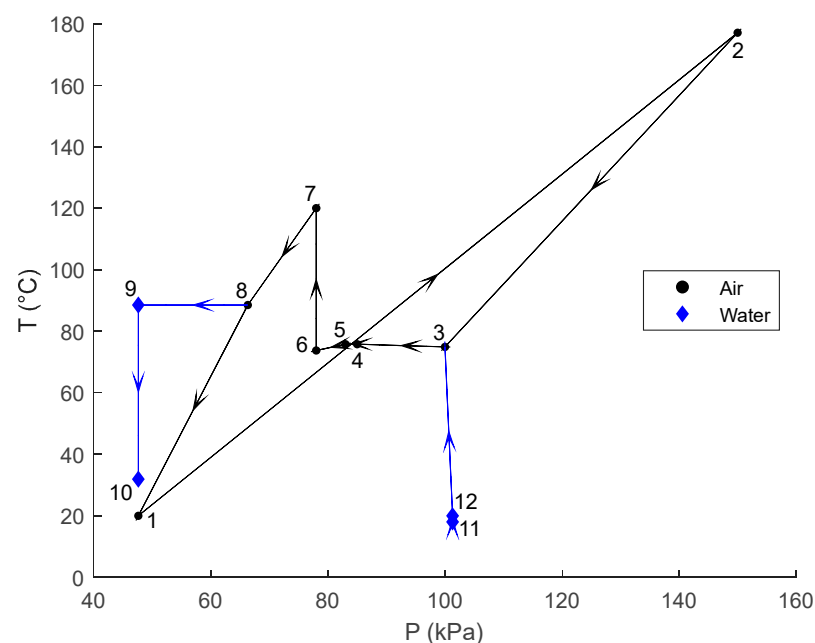


Figure 2. T-P diagram for the baseline cycle.

The atomized saline water-and-air stream (state 3) is evaporated at a temperature of 75 °C. At a water concentration of 100 g/kg, scaling is highly likely, as the operating temperature is close to the solubility limits of common scaling salts in desalination, such as CaSO_4 and CaCO_3 [52,53]. Although a small degree of CaCO_3 scaling can be beneficial by protecting equipment from corrosion [54], excessive scaling results in a lower overall heat transfer coefficient, which would prevent the achievement of full evaporation and

thus decrease performance of the system through reduced product quantity and quality (defined by low salinity). This can impede continuous operation of the system and incur additional operation costs. Measures such as feed pretreatment with scaling inhibitors [8,55], periodic cleaning, and novel engineering or material science solutions could be required for sustained system operation [56].

The separation process in the cyclone component does not incur major temperature changes (process 4–5–6). The moist air output from the cyclone (state 6) is superheated to a temperature of 120 °C, which supplies energy for condensation (process 7–8). The last significant temperature drop after the condensation process occurs in the air stream after the air–water separator. Considering the whole system, atomization is accountable for roughly half of the total pressure loss, followed by condensation and air–water separation, which are responsible for roughly one-third each. In the case of temperature, the differential incurred in the air stream through compression and atomization are the largest, followed by the temperature drop after removing water from the condensed mixture stream.

Figure 3 shows the humidity ratio and pressure changes in the air cycle within the system. Atomization alone accounts for almost half of the total air humidification in concurrence with the highest pressure drop. This is a unique characteristic in thermodynamic operation, as the thermal load conventionally used in driving distillation is offset by atomization. Atomization also acts as a facilitator for evaporation by substantially increasing available surface area for heat transfer. Moisture removal from the air, in contrast, occurs in a single step through cooling and dehumidification at the other side of the heat exchanger. The moisture content of the air stream after the separator must be controlled through the superheater temperature and separator design, as it could lead to corrosion in the compressor and losses in potentially recoverable freshwater product. Depending on ambient air conditions, implementing an open-air system could be a possibility that requires investigation for optimizing water recovery.

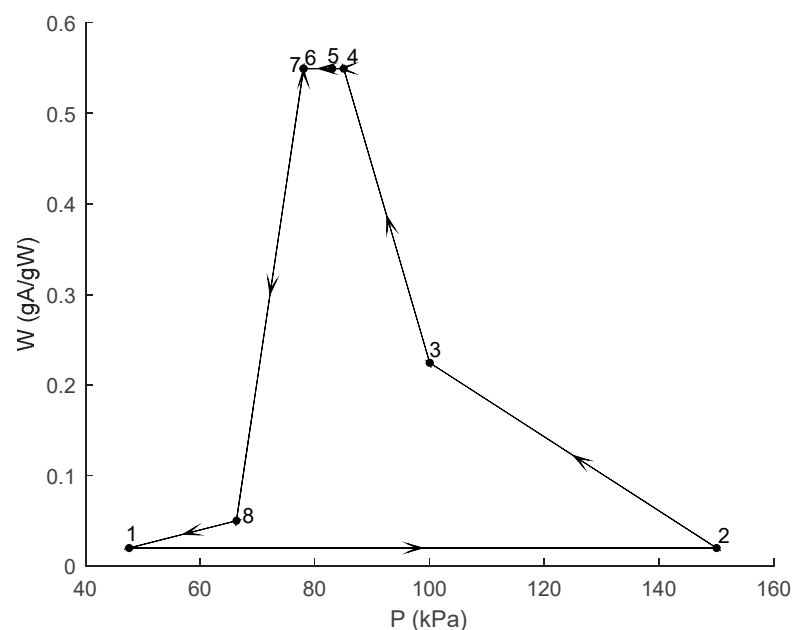


Figure 3. W-P diagram for the baseline cycle.

Figure 4 shows the enthalpy–pressure diagram for baseline operation. The greatest enthalpy changes occur between state points 3 and 4 and state points 7 and 8, which correspond to the evaporation and cooling–dehumidification processes. This is consistent with the energy increase in the system through the latent heat addition and removal of water in the air flow. Appropriate operation, therefore, is dependent on an effective heat exchanger, as it is the most critical component of the system. This contrasts the external

energy inputs that are associated with the smaller enthalpy changes through compression (state points 1–2) and superheating (state points 6–7).

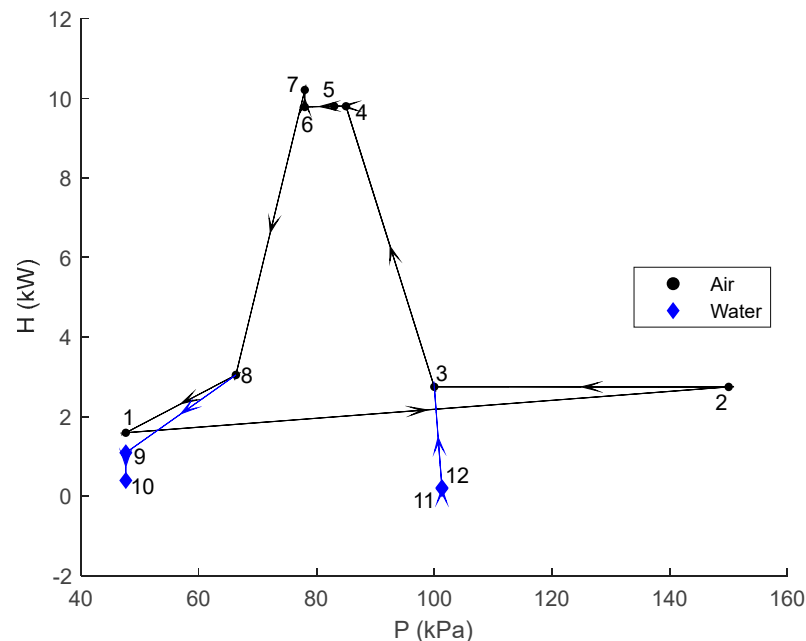


Figure 4. H-P diagram for baseline operation.

3.2. Sensitivity Analysis

In this section, the system model is used to conduct a sensitivity analysis to establish operation tradeoffs. A simple simulation engine is presented, which adjusts parameters in accordance with conservation and thermodynamic laws and bounds the simulation space by keeping the baseline parameters constant. The atomized water-and-air state (state point 3 in the cycle) is inferred by iterating through all possible temperatures between T_2 and T_{12} with $dT = 0.1$ °C and all possible air relative humidity values from 0 to 1 with a $d\phi = 0.01$. Deviating from baseline M_d or C_f usually results in a mismatch in energy across the evaporator, due either to a different latent load or boiling point elevation or to a violation in conservation laws across the atomizer as the amount of air required in atomization and moisture transport would vary. When this occurs, the simulation engine adjusts the air flow by ± 0.001 kg/s to approach the baseline air-to-water ratio of 1.8.

Figure 5 shows the system response for variations of $\pm 25\%$ and $\pm 75\%$ with respect to baseline M_d and C_f , respectively. The results highlight a safety overdesign in the air flow rate for maintaining full recovery. Decreasing product flow rate implies a lower latent load at the evaporator, which can be met by decreasing air flow rate if the baseline superheat temperature is kept constant. Decreasing M_d increases the contribution of the air stream in the total enthalpy during atomization as described by Equation (3). Since the state point at the compressor outlet is fixed, after around 20% decrease in water flow rate, the model must compensate the enthalpy contribution of water by decreasing the air flow. Thus, the air flow rate is directly proportional to decreasing M_d , and this is reflected in the linear compressor power change in the same direction. At higher water production rates, however, W_{comp} remains constant, as there is no need for the simulation engine to vary the air flow rate as the heat available after the superheater exceeds the heat required for evaporation, and the increased contribution of water to enthalpy mixture before and after atomization follows energy conservation. The heat required for evaporation (Q_{req}), conversely, is directly proportional to M_d , as higher water production increases the latent load in the evaporation process.

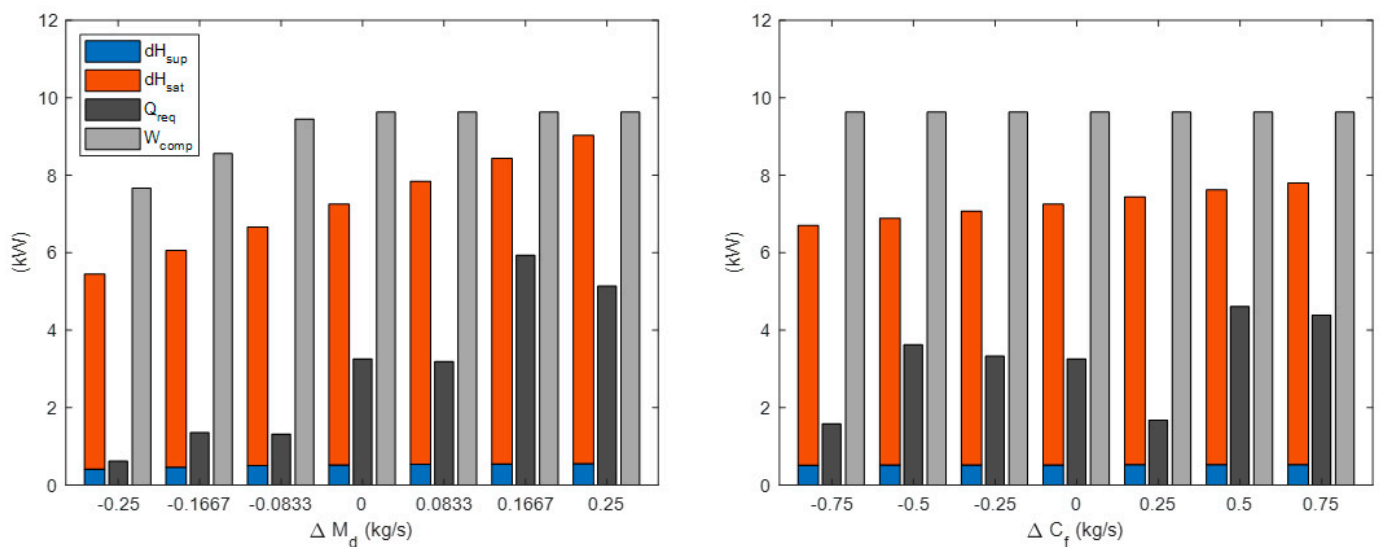


Figure 5. Sensitivity analysis results for M_d (left) and C_f (right).

Increasing feed salinity, on the other hand, indirectly increases feed water, as removing salt from higher concentrations results in less available water product. Furthermore, water transport increases since the operation must occur at higher temperatures, which are more favorable for moisture absorption. This makes targeting higher feed salinities plausible, as it also increases the product-water output without changing the compressor power. Furthermore, the available heat in the stream after superheater, consisting of the superheat path and the latent load at saturation, is consistently greater than the heat required for full evaporation at the other side of the heat exchanger by about 54% at baseline operation and at least 29% at higher-energy-demand scenarios caused by greater M_d or C_f . Thus, although higher salt content generally leads to boiling point elevation and greater heat required for evaporation, the excess heat input at baseline operation to the superheat portion overcomes the need for altering external heat inputs to the system. Therefore, Q_{req} and W_{comp} are practically independent from C_f if the rest of the parameters remain constant.

4. Discussion

While the thermodynamic analysis corroborates the physical viability of the STEWARD system, further simulations are conducted to investigate the possibility of replacing conventional desalination systems in actual plants or supplementing brine post-treatment. In this section, the implications of these deployment strategies are discussed, establishing the opportunities for STEWARD within the existing operational space of desalination methods.

4.1. Practical Operation

We assume multiple STEWARD units in parallel to fulfill large M_d values because adapting operation to a system whose target M_d exceeds the baseline by a factor of at least 10^3 is impractical. Obtaining an estimate of the number of units in parallel operation and the associated energy intensities, nonetheless, can help establish operational bounds that could guide further design iterations. Table 4 shows the operational costs assuming the implementation of enough STEWARD units in parallel to fulfill existing plant production requirements or process their corresponding brine product [46].

Table 4. STEWARD performance using case-study simulation data.

System Type	MDT	MDT	ROX	ROX
Plant Location	Jeddah, KSA	Jamnagar, IN	Bimini, BS	Cát Bà, VT
M_d (kg/s)	55	284	12	17
C_f (g/kg)	41.5	42	39	33
T_{in} (°C)	30	26	29	32
M_b (kg/s)	109	409	12	20
C_b (g/kg)	62.5	70	78.9	62.9
T_b (°C)	46	43	39	33
E_{des} (kWh/m ³)	132 _{th}	76 _{th}	2.7 _{el}	2.4 _{el}
Q_{req} (kW)	26,132	77,619	n/a	n/a
W_{pump} (kW)	n/a	n/a	110	149
RR (-)	0.34	0.41	0.50	0.47
STEWARD Replacement				
Total M_d (kg/s)	55	284	12	17
Units in Parallel	20,385	105,170	4449	6306
$E_{des}/unit$ (kWh/m ³)	1036	1036	1036	1012
$W_{comp}/unit$ (kW)	9.6	9.6	9.6	9.6
$dH_{sup}/unit$ (kW)	0.5	0.5	0.5	0.5
$Q_{req}/unit$ (kW)	3.0	2.9	1.6	2.1
RR/unit (-)	0.96	0.96	0.96	0.97
STEWARD Complement				
Total M_d (kg/s)	109	409	12	20
Units in Parallel	40,344	151,520	4442	7403
$E_{des}/unit$ (kWh/m ³)	1067	1069	1092	1072
$W_{comp}/unit$ (kW)	9.98	9.98	10.2	9.98
$dH_{sup}/unit$ (kW)	0.5	0.5	0.5	0.5
$Q_{req}/unit$ (kW)	1.3	1.7	1.1	1.4
RR/unit (-)	0.94	0.93	0.93	0.94

The high number of STEWARD units required to fulfill production rates and elevated energy intensity suggest that the proposed system may not replace existing desalination facilities but rather be a good supplement for brine processing. The latter scenario could be further supported if the brine is further concentrated into a hypersaline stream or if the STEWARD product-water flow rate is augmented such that fewer units in parallel are required. Current practices for brine disposal in the fracking industry range from 18 USD/m³ and 174 USD/m³ for surface disposal and existing deep-injection-well techniques, respectively, up to 7280 USD/m³ for lined evaporative pond methods [57]. Considering electricity rates in fracking states such as Texas (0.086 USD/kWh), West Virginia (0.1066 USD/kWh), and Pennsylvania (0.0981 USD/kWh), for cost comparison with STEWARD assuming electric heating, the baseline operation cost per unit would range between 72 USD/m³ and 96 USD/m³ [58].

4.2. Operational Map

The most relevant desalination methods include thermal processes such as TVC, MED, and HDH, as well as molecular transport processes including RO, Electrodialysis (EDS), and Capacitive Deionization (CDI). Figure 6 shows the operational space of existing desalination technologies compiled from plant data, bench scale systems, and models available in the literature [47]. The recovery achieved through HDH-ZLD is vastly different than conventional HDH methods, and therefore, it is considered as a standalone method. Thermal methods are usually associated with a higher energy intensity and low recovery ratios when compared to molecular transport methods. Furthermore, molecular transport methods are generally related to lower feed salinities due to high fouling tendencies [10,11].

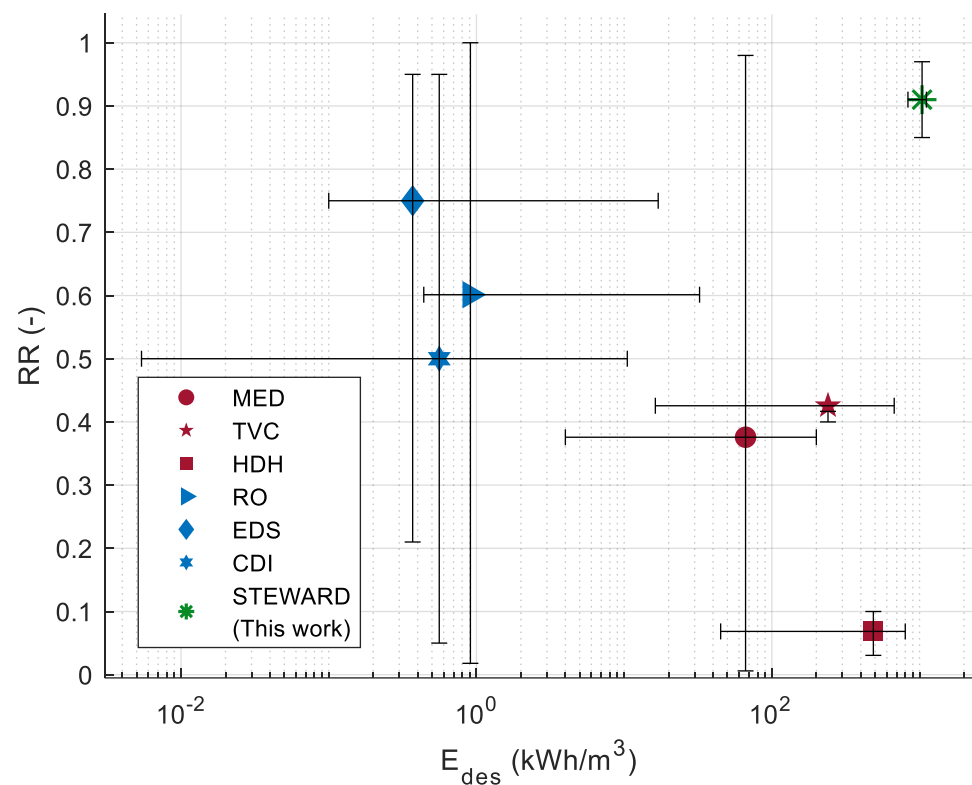


Figure 6. Operational map for different desalination technologies.

The achievable recovery rates of STEWARD are about 10 times larger than those achieved by conventional HDH processes, double the recovery reported in TVC methods, and comparable only to the high end of the recovery reported for MED. The practically full recovery ratio offered by STEWARD at baseline conditions could fulfill operation reported in the high recovery rate extremes within the molecular transport methods. Therefore, there is a niche in the operational space of desalination technologies characterized by the high recovery rates and high feed salinities that are generally unfulfilled by conventional desalination methods.

The map represents potential operation ranges based on first principles, including mass balance of water, salt, and air, as well as conservation of energy. The actual operational ranges would depend on system component performance and could require more energy than predicted in this analysis due to system inefficiencies. Nevertheless, if an inexpensive energy source is available, the STEWARD system could process high-salinity brines with almost complete water recovery.

The total energy intensity associated with STEWARD is comparable to the higher end of the energy intensity reported in other thermal methods. About 50 kWh/m³ corresponds to thermal energy input to the superheater, which matches the midrange point of the thermal energy intensity of MED desalination and lies at the lower ranges of TVC and HDH desalination. This implies that most energy is required in atomization (about 95%), which facilitates and integrates ZLD within the desalination process, in contrast with the energy intensity associated with the conventional desalination methods presented in Figure 6, which represents the desalination process alone at lower feed salinities. The energy loss in atomization is reflected in the pressure drop across the component; therefore, the competitiveness of the STEWARD system in the marketplace is contingent upon efficient atomizer design and performance. The presence of the compressor implies that the current STEWARD concept must depend on electricity alone or electricity and heat to operate. This could potentially be an important factor when considering locations for deployment. From an operational perspective, adoption of the STEWARD system would ultimately be associated with the costs of energy available and brine management at the desalination site.

5. Conclusions

In this paper, we presented a thermodynamic model for a novel HDH-based process with ZLD capabilities embodied in a Solar Thermal Extraction of Water by Atomization and Recuperative Desalination (STEWARD) system. First-principles modeling can bound system operation based on conservation laws and find plausible operation states. This analysis identified potential contingencies, including the pressure drop of the atomization process and scaling at the evaporator side of the heat exchanger, which must continue to be addressed throughout the development process. A sensitivity analysis was conducted to identify the tradeoffs associated with changes in feed salinity and freshwater production to map out the operational space in which the technology could be deployed. Unlike conventional technologies, such as RO and MED, the energy intensity in the STEWARD system is minimally sensitive to changes in C_f . In addition, its configuration allows for variation in M_d without incurring additional external energy inputs. The resulting energy intensity is slightly higher than conventional desalination methods. However, the system can achieve almost complete recovery from hypersaline feeds, which is an area of operation that is not traditionally served by other well-established desalination processes. The total operation utility cost associated with the energy intensity is expected to be comparable with current brine management and disposal practices. The crux of the proposed STEWARD system lies at the achievable product flow rates, which could challenge scalability. The presented first-principles model can be refined once system data become available to incorporate predictive physics-based and data-driven approaches to bring the STEWARD concept towards a pilot plant deployment.

Author Contributions: Conceptualization, S.A.R. and J.S.; Methodology, S.A.R. and M.E.; Software, S.A.R.; Validation, S.A.R.; Formal Analysis, S.A.R.; Investigation, S.A.R. and M.E.; Resources, J.S.; Data Curation, S.A.R.; Writing—Original Draft Preparation, S.A.R. and M.E.; Writing—Review and Editing, S.A.R. and J.S.; Visualization, S.A.R. and J.S.; Supervision, B.A. and J.S.; Project Administration, B.A. and J.S.; Funding Acquisition, B.A. and J.S. All authors have read and agreed to the published version of the manuscript.

Funding: This research was funded by the U.S. Department of Energy Office of Energy Efficiency and Renewable Energy, grant number DE-EE0008402.

Data Availability Statement: Model and simulation engine source code openly available online at: <https://desal.city.umd.edu>.

Conflicts of Interest: The authors declare no conflict of interest. The sponsors had no role in the design, execution, interpretation, or writing of the study.

References

1. Ahmed, F.E.; Khalil, A.; Hilal, N. Emerging Desalination Technologies: Current Status, Challenges and Future Trends. *Desalination* **2021**, *517*, 115183. [[CrossRef](#)]
2. Lin, S.; Zhao, H.; Zhu, L.; He, T.; Chen, S.; Gao, C.; Zhang, L. Seawater Desalination Technology and Engineering in China: A Review. *Desalination* **2021**, *498*, 114728. [[CrossRef](#)]
3. Al-Ahmad, M.; Aleem, F.A. Scale Formation and Fouling Problems and Their Predicted Reflection on the Performance of Desalination Plants in Saudi Arabia. *Desalination* **1994**, *96*, 409–419. [[CrossRef](#)]
4. Mavukkandy, M.O.; Chabib, C.M.; Mustafa, I.; Al Ghaferi, A.; AlMarzooqi, F. Brine Management in Desalination Industry: From Waste to Resources Generation. *Desalination* **2019**, *472*, 114187. [[CrossRef](#)]
5. Antony, A.; Low, J.H.; Gray, S.; Childress, A.E.; Le-Clech, P.; Leslie, G. Scale Formation and Control in High Pressure Membrane Water Treatment Systems: A Review. *J. Memb. Sci.* **2011**, *383*, 1–16. [[CrossRef](#)]
6. Al-Karaghoul, A.; Kazmerski, L.L. Energy Consumption and Water Production Cost of Conventional and Renewable-Energy-Powered Desalination Processes. *Renew. Sustain. Energy Rev.* **2013**, *24*, 343–356. [[CrossRef](#)]
7. Wenten, I.G.; Aryanti, P.T.P.; Hakim, A.N. Scale-up Strategies for Membrane-Based Desalination Processes: A Review. *J. Membr. Sci. Res.* **2016**, *2*, 42–58. [[CrossRef](#)]
8. Sutzkover-Gutman, I.; Hasson, D. Feed Water Pretreatment for Desalination Plants. *Desalination* **2010**, *264*, 289–296. [[CrossRef](#)]
9. Kavitha, J.; Rajalakshmi, M.; Phani, A.R.; Padaki, M. Pretreatment Processes for Seawater Reverse Osmosis Desalination Systems—A Review. *J. Water Process Eng.* **2019**, *32*, 100926. [[CrossRef](#)]

10. Goh, P.S.; Lau, W.J.; Othman, M.H.D.; Ismail, A.F. Membrane Fouling in Desalination and Its Mitigation Strategies. *Desalination* **2018**, *425*, 130–155. [CrossRef]
11. She, Q.; Wang, R.; Fane, A.G.; Tang, C.Y. Membrane Fouling in Osmotically Driven Membrane Processes: A Review. *J. Memb. Sci.* **2016**, *499*, 201–233. [CrossRef]
12. Hoek, E.M.V.; Allred, J.; Knoell, T.; Jeong, B.-H. Modeling the Effects of Fouling on Full-Scale Reverse Osmosis Processes. *J. Memb. Sci.* **2008**, *314*, 33–49. [CrossRef]
13. Jafari, M.; Vanoppen, M.; van Agtmaal, J.M.C.; Cornelissen, E.R.; Vrouwenvelder, J.S.; Verliefe, A.; van Loosdrecht, M.C.M.; Picioreanu, C. Cost of Fouling in Full-Scale Reverse Osmosis and Nanofiltration Installations in the Netherlands. *Desalination* **2021**, *500*, 114865. [CrossRef]
14. Panagopoulos, A.; Haralambous, K.J.; Loizidou, M. Desalination Brine Disposal Methods and Treatment Technologies—A Review. *Sci. Total Environ.* **2019**, *693*, 133545. [CrossRef]
15. Essa, F.A.; Abdullah, A.S.; Omara, Z.M.; Kabeel, A.E.; El-Maghlany, W.M. On the Different Packing Materials of Humidification-Dehumidification Thermal Desalination Techniques—A Review. *J. Clean. Prod.* **2020**, *277*, 123468. [CrossRef]
16. Ahmadvand, S.; Abbasi, B.; Azarfar, B.; Elhashimi, M.; Zhang, X.; Abbasi, B. Looking Beyond Energy Efficiency: An Applied Review of Water Desalination Technologies and an Introduction to Capillary-Driven Desalination. *Water* **2019**, *11*, 696. [CrossRef]
17. Heck, N.; Lykkebo Petersen, K.; Potts, D.C.; Haddad, B.; Paytan, A. Predictors of Coastal Stakeholders' Knowledge about Seawater Desalination Impacts on Marine Ecosystems. *Sci. Total Environ.* **2018**, *639*, 785–792. [CrossRef]
18. Ahmad, N.; Baddour, R.E. A Review of Sources, Effects, Disposal Methods, and Regulations of Brine into Marine Environments. *Ocean Coast. Manag.* **2014**, *87*, 1–7. [CrossRef]
19. Yaqub, M.; Lee, W. Zero-Liquid Discharge (ZLD) Technology for Resource Recovery from Wastewater: A Review. *Sci. Total Environ.* **2019**, *681*, 551–563. [CrossRef]
20. Cipolletta, G.; Lancioni, N.; Akyol, Ç.; Eusebi, A.L.; Fatone, F. Brine Treatment Technologies towards Minimum/Zero Liquid Discharge and Resource Recovery: State of the Art and Techno-Economic Assessment. *J. Environ. Manage.* **2021**, *300*, 113681. [CrossRef]
21. Abbasi, B.; Khalifa, M.A.E.; Sharma, D.; Zhang, X. Method and Apparatus for Desalinating Water. US Patent 0039008A1, 11 February 2021. Available online: <https://patents.google.com/patent/US20210039008A1/en> (accessed on 27 July 2022).
22. Alsehli, M. A New Approach to Solar Desalination Using a Humidification–Dehumidification Process for Remote Areas. *Processes* **2021**, *9*, 1120. [CrossRef]
23. Santosh, R.; Kumaresan, G.; Selvaraj, S.; Arunkumar, T.; Velraj, R. Investigation of Humidification-Dehumidification Desalination System through Waste Heat Recovery from Household Air Conditioning Unit. *Desalination* **2019**, *467*, 1–11. [CrossRef]
24. Elhashimi, M.A.; Zhang, X.; Abbasi, B. Empirical Prediction of Saline Water Atomization Pressure Loss and Spray Phase Change Using Local Flow Pressure Analysis. *Desalination* **2021**, *514*, 115156. [CrossRef]
25. Sharma, D.; Ghosh, D.P.; Rote, J.N.; Dennis, S.J.; Messer, M.; Zhang, X.; Abbasi, B. Development of an Anti-Clogging Perforated Plate Atomizer for a Zero Liquid Discharge Humidification-Dehumidification Desalination System. *Desalination* **2021**, *515*, 115195. [CrossRef]
26. Elhashimi, M.A.; Shorb, J.; Messer, M.; Abbasi, B. Assessment of Humid Air-Solids Cyclone Separators in A Novel Humidification-Dehumidification Desalination. In Proceedings of the IDA International Water Reuse and Recycling Conference, Rome, Italy, 11–13 October 2021.
27. Jedelsky, J.; Jicha, M. Energy Conversion during Effervescent Atomization. *Fuel* **2013**, *111*, 836–844. [CrossRef]
28. Hoffmann, A.C.; Stein, L.E. *Gas Cyclones and Swirl Tubes*; Springer: Berlin/Heidelberg, Germany, 2007; ISBN 978-3-540-74694-2.
29. de Nevers, N. *Air Pollution Control Engineering*, 2nd ed.; McGraw-Hill: Boston, MA, USA, 2000; ISBN 978-0070393677.
30. Elhashimi, M.A.; Gee, M.; Abbasi, B. Unconventional Desalination: The Use of Cyclone Separators in HDH Desalination to Achieve Zero Liquid Discharge. *Desalination* **2022**, *539*, 115932. [CrossRef]
31. Sharma, D.; Ghosh, D.P.; Dennis, S.J.; Abbasi, B. Fouling Mechanism in Airblast Atomizers and Its Suppression for Water Desalination. *Water Res.* **2022**, *221*, 118726. [CrossRef]
32. Ochowiak, M.; Matuszak, M.; Włodarczyk, S.; Krupińska, A.; Markowska, M.; Gościński, A.; Szulc, T. The Concept Design and Study of Twin-Fluid Effervescent Atomizer with Air Stone Aerator. *Chem. Eng. Process. Process Intensif.* **2018**, *124*, 24–28. [CrossRef]
33. Kourmatzis, A.; Lowe, A.; Masri, A.R. Combined Effervescent and Airblast Atomization of a Liquid Jet. *Exp. Therm. Fluid Sci.* **2016**, *75*, 66–76. [CrossRef]
34. Tesař, V. New Concept: Low-Pressure, Wide-Angle Atomiser. *Chem. Eng. Process. Process Intensif.* **2014**, *82*, 19–29. [CrossRef]
35. Abdelaziz, G.B.; Dahab, M.A.; Omara, M.A.; Sharshir, S.W.; Elsaid, A.M.; El-Said, E.M.S. Humidification Dehumidification Saline Water Desalination System Utilizing High Frequency Ultrasonic Humidifier and Solar Heated Air Stream. *Therm. Sci. Eng. Prog.* **2022**, *27*, 101144. [CrossRef]
36. Tourab, E.A.; Blanco-Marigorta, A.M.; Elharidi, A.M.; Suárez-López, M.J. A Novel Humidification Technique Used in Water Desalination Systems Based on the Humidification–Dehumidification Process: Experimentally and Theoretically. *Water* **2020**, *12*, 2264. [CrossRef]
37. Soomro, S.H.; Santosh, R.; Bak, C.U.; Kim, W.S.; Kim, Y.D. Humidification–Dehumidification Desalination System Powered by Simultaneous Air–Water Solar Heater. *Sustainability* **2021**, *13*, 13491. [CrossRef]

38. Xiong, Z.; Lu, M.; Wang, M.; Gu, H.; Cheng, X. Study on Flow Pattern and Separation Performance of Air-Water Swirl-Vane Separator. *Ann. Nucl. Energy* **2014**, *63*, 138–145. [[CrossRef](#)]
39. SFitz. AirProperties. Available online: <https://github.com/sjfitz/AirProperties> (accessed on 27 July 2022).
40. Picard, A.; Davis, R.S.; Gläser, M.; Fujii, K. Revised Formula for the Density of Moist Air (CIPM-2007). *Metrol* **2008**, *45*, 149–155. [[CrossRef](#)]
41. Tsilingiris, P.T. Thermophysical and Transport Properties of Humid Air at Temperature Range between 0 and 100 °C. *Energy Convers. Manag.* **2008**, *49*, 1098–1110. [[CrossRef](#)]
42. Miller, J. Ideal Air Properties. Available online: <https://www.mathworks.com/matlabcentral/fileexchange/25030-ideal-air-properties> (accessed on 24 November 2020).
43. Nayar, K.G.; Sharqawy, M.H.; Banchik, L.D.; Lienhard, J.H. Thermophysical Properties of Seawater: A Review and New Correlations That Include Pressure Dependence. *Desalination* **2016**, *390*, 1–24. [[CrossRef](#)]
44. Sharqawy, M.H.; Lienhard, J.H.; Zubair, S.M. Thermophysical Properties of Seawater: A Review of Existing Correlations and Data. *Desalin. Water Treat.* **2010**, *16*, 354–380. [[CrossRef](#)]
45. Holmgren, M. X Steam, Thermodynamic Properties of Water and Steam. Available online: <https://www.mathworks.com/matlabcentral/fileexchange/9817-x-steam-thermodynamic-properties-of-water-and-steam> (accessed on 27 July 2022).
46. Romo, S.A.; Storch, M., Jr.; Srebric, J. Operation Modeling of Actual Desalination Plants. *Desalination* **2022**, *Under peer-review.*
47. Romo, S.A.; Mattise, N.; Srebric, J. Desalination Metamodels and a Framework for Cross-Comparative Performance Simulations. *Desalination* **2022**, *525*, 115474. [[CrossRef](#)]
48. Ettouney, H. Design and Analysis of Humidification Dehumidification Desalination Process. *Desalination* **2005**, *183*, 341–352. [[CrossRef](#)]
49. Sharqawy, M.H.; Antar, M.A.; Zubair, S.M.; Elbashir, A.M. Optimum Thermal Design of Humidification Dehumidification Desalination Systems. *Desalination* **2014**, *349*, 10–21. [[CrossRef](#)]
50. Farsad, S.; Behzadmehr, A.; Sarvari, S.M.H. Numerical Analysis of Solar Desalination Using Humidification—Dehumidification Cycle. *Desalin. Water Treat.* **2010**, *19*, 294–300. [[CrossRef](#)]
51. Prihatiningtyas, I.; Al-Kebsi, A.H.A.H.; Hartanto, Y.; Zewdie, T.M.; Van der Bruggen, B. Techno-Economic Assessment of Pervaporation Desalination of Hypersaline Water. *Desalination* **2022**, *527*, 115538. [[CrossRef](#)]
52. Jin, H.Q.; Shahane, S.; Zhang, Y.; Wang, S.; Nawaz, K. Modeling of Crystallization Fouling on a Horizontal-Tube Falling-Film Evaporator for Thermal Desalination. *Int. J. Heat Mass Transf.* **2021**, *178*, 121596. [[CrossRef](#)]
53. El-Dessouky, H.T.; Ettouney, H.M.; Mandani, F. Performance of Parallel Feed Multiple Effect Evaporation System for Seawater Desalination. *Appl. Therm. Eng.* **2000**, *20*, 1679–1706. [[CrossRef](#)]
54. Hodgkiess, T. Inter-Relationships between Corrosion and Mineral-Scale Deposition in Aqueous Systems. *Water Sci. Technol.* **2004**, *49*, 121–128. [[CrossRef](#)] [[PubMed](#)]
55. Chaussemier, M.; Pourmohtasham, E.; Gelus, D.; Pécou, N.; Perrot, H.; Lédion, J.; Cheap-Charpentier, H.; Horner, O. State of Art of Natural Inhibitors of Calcium Carbonate Scaling. A Review Article. *Desalination* **2015**, *356*, 47–55. [[CrossRef](#)]
56. Fellows, C.M.; Al Hamzah, A.A.; East, C.P. Scale Control in Thermal Desalination. In *Water-Formed Deposits: Fundamentals and Mitigation Strategies*, 1st ed.; Amjad, Z., Demadis, K.D., Eds.; Elsevier: Amsterdam, The Netherlands, 2022; pp. 457–476.
57. Ziemkiewicz, P.; Hause, J.; Lovett, R.; Harry Johnson, D.L.; Patchen, D. Zero Discharge Water Management for Horizontal Shale Gas Well Development. Available online: <http://www.osti.gov/servlets/purl/1054519/> (accessed on 27 July 2022).
58. US Energy Information Administration Electric Sales, Revenue, and Average Price. Available online: https://www.eia.gov/electricity/sales_revenue_price/ (accessed on 6 January 2021).